

Hybrid Quantum Physics-informed Neural Network: Towards Efficient Learning of High-speed Flows

Fong Yew Leong ^{*}1, Wei-Bin Ewe ¹, Tran Si Bui Quang ¹, Zhongyuan Zhang¹, and Jun Yong Khoo ¹

¹Institute of High Performance Computing (IHPC), Agency for Science, Technology and Research (A*STAR), 1 Fusionopolis Way, #16-16 Connexis, Singapore 138632, Singapore

March 5, 2025

Abstract

This study assesses the potential use of hybrid quantum physics-informed neural network (HQPINN) to model high-speed flows as an alternative to classical PINN and quantum neural network options. The model integrates parameterized quantum circuit (PQC) with classical neural network in parallel as input to a physics-based optimization. For problems with harmonic solutions, the HQPINN exhibits superior accuracy and trainability compared to both classical and quantum models at low parameter costs. For transonic flows, the hybrid approach yields modest results and additionally suffers from poor trainability if the quantum layer were under-parameterized. Our results highlight inherent limitations in deploying quantum neural networks in PINN applications, and potential use of hybrid architectures as a general tool in problems where the nature of the solution is not known *a-priori*.

1 Introduction

Prediction of compressible air flow features at transonic speed is critical to efficient aerofoil design. This problem involves solving a nonlinear set of partial differential equations (PDEs) in a domain bound by an irregular aerofoil geometry, aspects which pose formidable challenge to traditional computational fluid dynamics (CFD) [1]. In recent years, machine learning techniques, particularly physics-informed neural networks (PINNs) [2], have emerged as a promising tool for handling high-speed flows, with certain advantages in data-driven neural networks and inverse applications [3–6].

Conceptually, PINNs use differentiable neural networks to approximate the solution of some governing equations, in a way that obeys imposed physical laws, including nonlinear phenomena and geometric constraints [2]. This approach allows for the incorporation of prior physical knowledge directly into the learning process, enhancing the model’s ability to generalize from limited data. However, as a neural network strategy, PINNs are also limited by extensive use of automatic differentiation for training, which often leads to long training times and prohibitive computational costs [6].

Quantum computing [7] offers a promising avenue to accelerate scientific computing and machine learning, particularly through quantum machine learning (QML) [8]. QML performs machine learning tasks on a parameterized quantum circuit (PQC), also known as quantum neural network, which exploits quantum features such as superposition and entanglement for higher trainability and expressivity [9]. PQCs are not only universal approximators like classical multi-layered perceptrons (MLPs), but they also act as truncated Fourier series models [10]. This unique feature enables PQCs to capture complex patterns and relationships in data more efficiently than classical models.

^{*}Corresponding author.

Recent studies have seen efforts to replace classical neural networks with quantum PQC, either partially or entirely. For instance, Arthur and Date [11] proposed a hybrid quantum neural network consisting of a quantum PQC layer and a classical MLP layer in series for classification problems showing a higher accuracy compared to pure PQC. Kordzanganeh et al. [12] proposed a parallel hybrid quantum neural network of extracting both harmonic and non-harmonic features from a dataset [13]. Since then, there are studies of hybrid classical-quantum neural networks modeling flows past a cylinder [14] and mixing flows via transfer learning [15]. More recently, Xiao et al. [16] simulated quantum neural networks for partial differential equations, which can deliver high accuracy solutions using fewer trainable parameters.

In this study, we explore the use of hybrid quantum PINN (HQPINN) on high-speed flows problems. This is a challenging CFD problem where pure quantum neural networks are *not favored* due to non-harmonic solutions that include shocks and discontinuities [16]. We argue that, in the absence of detailed prior knowledge of the problem, a hybrid quantum PINN could flexibly model flows that include both smooth and discontinuous features. For verification, we assess the use of HQPINNs on model problems by benchmarking their trainability and training accuracy against classical PINNs and PQCs with varying complexities.

2 Methodology

2.1 Governing equations

For 2D inviscid compressible flow, the governing Euler equations are [3, 4]:

$$\partial_t U + \nabla \cdot G(U) = 0, \quad \mathbf{x} := (x, y) \in \Omega \subset \mathbb{R}^2, \quad t \in (0, T], \quad (1)$$

where

$$U = \begin{pmatrix} \rho \\ \rho u \\ \rho v \\ \rho E \end{pmatrix}, \quad G = \{G_1, G_2\}, \quad G_1(U) = \begin{pmatrix} \rho u \\ p + \rho u^2 \\ \rho uv \\ pu + \rho uE \end{pmatrix}, \quad G_2(U) = \begin{pmatrix} \rho v \\ \rho uv \\ p + \rho v^2 \\ pv + \rho vE \end{pmatrix},$$

ρ is the fluid density, (u, v) are velocity components in (x, y) , E is the total energy and p is the pressure. The equation of state for a polytropic gas is

$$p = (\gamma - 1) \left(\rho E - \frac{1}{2} \rho \|\mathbf{u}\|^2 \right), \quad (2)$$

where $\gamma = 1.4$ is the ratio of specific heats for air, and $\mathbf{u} = (u, v)$. The pressure p also satisfies the ideal gas law $p = \rho RT$, where T is the temperature and R is the ideal gas constant ($287 \text{ J kg}^{-1} \text{ K}^{-1}$ for air). Under steady state conditions, Eq. 1 simplifies to

$$\nabla \cdot G(U) = 0, \quad \{x, y\} \in \Omega. \quad (3)$$

2.2 Physics-informed neural networks

The physics-informed neural network (PINN) consists of an uninformed neural network aiming to satisfy data states including initial and boundary conditions, and an informed neural network aiming to satisfy conservation laws Eq. 1, both networks sharing hyper-parameters. Let us define

$$F(\mathbf{x}, t) = \partial_t U_{NN}(\mathbf{x}, t) + \nabla \cdot G(U_{NN}(\mathbf{x}, t)), \quad (4)$$

where $U_{NN}(\mathbf{x}, t)$ is the approximation of U by using a deep neural network. The derivative of the deep neural network can be computed using auto differentiation. The parameters of $U_{NN}(\mathbf{x}, t)$ can then be learned by minimizing the loss function

$$\mathcal{L} = \mathcal{L}_{BC} + \mathcal{L}_F, \quad (5)$$

where \mathcal{L}_{BC} is the data loss, including initial and boundary conditions, and \mathcal{L}_F is the physics loss in Eq. 4. Using mean-squared-error (MSE), the respective loss functions can be minimized via

$$\mathcal{L}_{BC} = \frac{1}{N_B} \sum_{j=1}^{N_B} |U_{NN}(\mathbf{x}_j^B, t_j^B) - U(\mathbf{x}_j^B, t_j^B)|^2, \quad (6)$$

$$\mathcal{L}_F = \frac{1}{N_F} \sum_{j=1}^{N_F} |F(\mathbf{x}_j^F, t_j^F)|^2, \quad (7)$$

where $\{\mathbf{x}_j^B, t_j^B\}_{j=1}^{N_B}$ are initial and boundary collocation points with N_B number of points, and $\{\mathbf{x}_j^F, t_j^F\}_{j=1}^{N_F}$ are collocation points for $F(\mathbf{x}, t)$ with N_F number of points.

2.3 Parameterized quantum circuit

Quantum machine learning (QML) is the application of quantum computing to machine learning tasks [17]. In the literature, QML circuits are also often referred to as variational quantum circuits, quantum circuit learning, quantum neural networks or parameterized quantum circuits (PQC).

At its core, a PQC implements a quantum model function $f(\boldsymbol{\theta}, \boldsymbol{\varphi})$ by constructing a quantum circuit using fixed gates that encode N data inputs or features $\boldsymbol{\varphi} = (\varphi_1, \dots, \varphi_N)$ and variational gates with M trainable weights $\boldsymbol{\theta} = (\theta_1, \dots, \theta_M)$. Using Dirac notations, the expectation of some observable \mathcal{O} can be measured using the Born rule as

$$f(\boldsymbol{\theta}, \boldsymbol{\varphi}) = \langle \psi(\boldsymbol{\theta}, \boldsymbol{\varphi}) | \mathcal{O} | \psi(\boldsymbol{\theta}, \boldsymbol{\varphi}) \rangle, \quad (8)$$

where $|\psi(\boldsymbol{\theta}, \boldsymbol{\varphi})\rangle$ is the quantum state at the point of measurement. Note that the quantum model fits a truncated Fourier series function [10], as

$$f(\boldsymbol{\varphi}) = \sum_{k=-L}^L c_k e^{ik\boldsymbol{\varphi}}, \quad (9)$$

where L is the highest degree of the Fourier series.

Like a multi-layered perceptron (MLP), a PQC is also an universal approximator that can functionally replace at least parts of a neural network, forming a classical-quantum interface known as hybrid quantum neural network (HQNN) [13]. There are a few reasons why this might be a good idea. Quantum computers already offer exponential computational capacity over classical computers in the form of a large Hilbert space and may also enhance the machine learning process [18]. Also, the tools of differential quantum circuits [19] align with classical neural networks using automatic differentiation and back-propagation. Finally, the Fourier model of a PQC (Eq. 9) could extract harmonic features from a suitable dataset and complement a classical neural network [13].

2.4 Hybrid quantum physics-informed neural networks

Here, we propose a hybrid quantum physics-informed neural network (HQPINN) as sketched in Figure 1. The HQPINN samples (x, t) data and output $\{\rho, u, p\}$ using a hybrid architecture with quantum and classical layers arranged in parallel [13]:

Quantum layer An $n = 3$ qubit PQC formed by alternating $l - 1$ layers of feature map $S(\boldsymbol{\varphi})$ and parameterized ansatz $A(\boldsymbol{\theta})$ in the following sequence: $A - (S - A)_1 - \dots - (S - A)_{l-1}$. Data encoding follows a data-reuploading scheme via angle encoding of the input n -node classical layer $\varphi_{1-3} \mapsto S(\boldsymbol{\varphi})$. Refer to Appendix A.1 for details on quantum circuit design. Pauli-Z expectation measurements are performed on each qubit $q_i = \langle Z_i \rangle$, where $i = [1, n]$, leading to an n node output layer $q_{[1, n]}$.

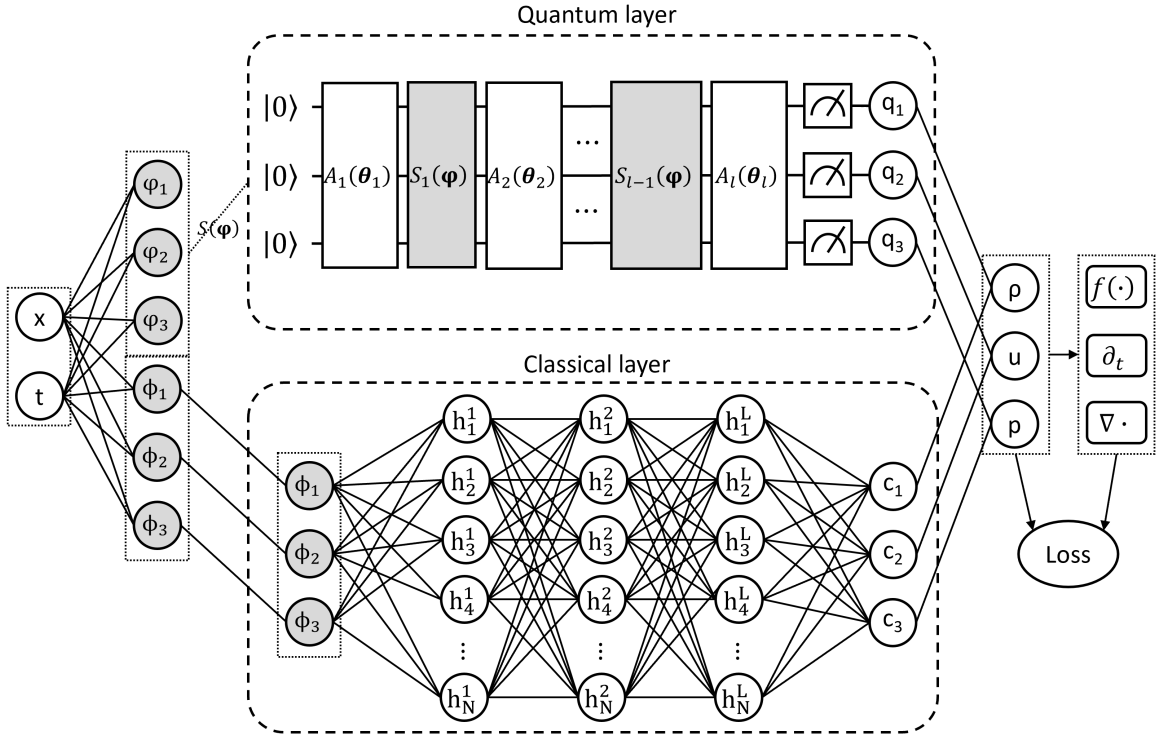


Figure 1: Schematic of proposed HQPINN which samples (x, t) data into a parallel architecture coupling a quantum layer (top), an n qubit PQC formed by alternating $l - 1$ layers of feature map $S(\boldsymbol{\varphi})$ and l layers of parameterized ansatz $A(\boldsymbol{\theta})$, with a classical layer (bottom), a neural network formed by an input layer with n nodes and L hidden layers of N nodes [13]. The quantum output $q_{[1,n]}$ and classical output $c_{[1,n]}$ combine linearly to approximate (ρ, u, p) and their informed functions $(f(\cdot), \partial_t, \nabla \cdot)$, both collectively contribute towards a loss function for optimization [3].

Classical layer Neural network with (x, t) data passed to a n -node input layer $\phi_{[1,n]}$ with bias and tanh activation function applied. This is followed by L hidden layers of N nodes, before a n -node output layer $c_{[1,n]}$.

The final neural network layer is a weighted linear combination of the outputs from the quantum and classical layers $o_i = s_i^c c_i + s_i^q q_i$ [12] to produce an output vector $\{\rho, u, p\}$ for minimization of the loss function Eq. 5. We tested the hybrid classical–quantum neural network (Fig. 1) against a classical–classical neural network where the parallel network layers are both classical layers, and a quantum–quantum neural network where the parallel network layers are both quantum layers. For the introductory 1D harmonic oscillator problem, the HQPINN was found to outperform both classical–classical and quantum–quantum neural network architectures (Appendix A.2). Henceforth, we aim to verify if the hybrid classical–quantum scheme holds up for more challenging problems such as high-speed shock flows.

3 Numerical results

We test and compare classical and quantum PINN models based on two example cases on high-speed flows, one with smooth solutions ([3], example 6) and the other with discontinuous solutions ([3], example 1). Here we consider three models:

Classical–classical(cc) Parallel classical layers each 4 or 7 hidden layers and 10 or 20 nodes per layer.

Quantum–quantum(qq) Parallel quantum layers each 3 qubits with 2 or 4 layers.

Classical–quantum(hy) Hybrid parallel classical and quantum layers (see Fig. 1).

For convenience, we adopt the following itemized notation for each model. The label *cc* denotes classical model, followed by the number of nodes per hidden layer and the number of hidden layers respectively. The label *qq* denotes quantum model, followed by number of trainable layers. The label *hy* denotes hybrid classical–quantum model, followed by the number of nodes per hidden layer, the number of hidden layers and number of trainable quantum layers respectively.

Models are implemented on *Pytorch* [20] interfaced with *Pennylane* [21] and run on distributed CPU without GPU acceleration. Loss functions (Eq. 5) are minimized via mean square error (Eq. 6 and 7) using Adam optimizer for 20 000 steps with learning rate 0.0005. The quantum layer is simulated classically, which results in an actual compute time that is slower than a classical layer by at least an order of magnitude[16].

3.1 Smooth Euler

Consider a 1D Euler equation with smooth solution ([3], example 6). We use periodic boundary conditions and initial condition,

$$U_0 = (\rho_0, u_0, p_0) = (1.0 + 0.2 \sin(\pi x), 1.0, 1.0), \quad (10)$$

which leads to a traveling wave solution

$$(\rho, u, p) = (1.0 + 0.2 \sin(\pi(x - t)), 1.0, 1.0), \quad (11)$$

in a domain defined by $x \in (-1, 1)$ and $t \in (0, 2)$. Following ([3], example 6), we randomly sample $N_{ic} = 50$, $N_{bc} = 50$ and $N_F = 2000$ training points for initial condition *ic*, boundary condition *bc* (Eq. 6) and domain *F* (Eq. 7) respectively.

Figure 2 shows a traveling wave solution of the density based on classical *cc-10-4* model, with high fidelity agreement with the exact solution indicated by their normalized deviation. Table 1 compares the number of trainable parameters required for each model and the resultant loss and error at the 20 000th

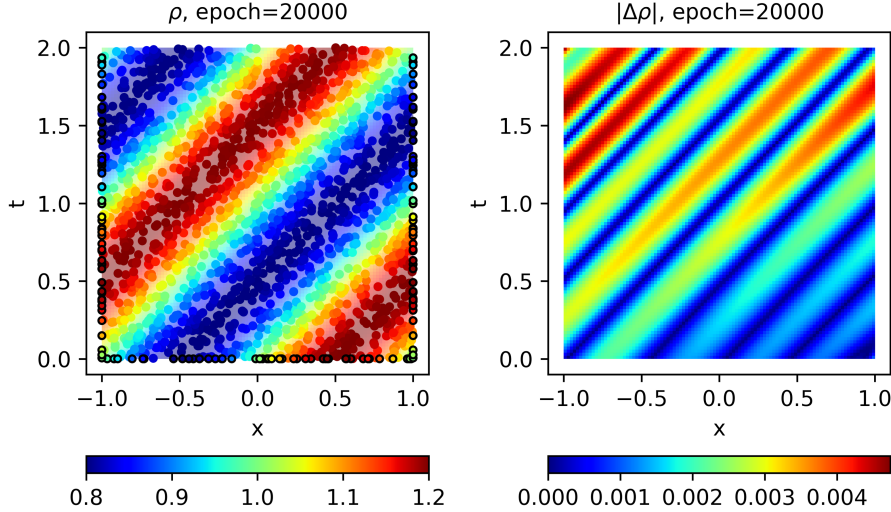


Figure 2: Plot of smooth traveling wave solution for 1D Euler equation (Section 3.1). (Left) Density in x - t domain. Opaque bubbles are domain residual training points and dark circled bubbles are boundary data training points. (Right) Normalized deviation from exact solution (Eq. 11).

epoch. Here, the best model is the quantum qq -2 model with an average loss of 2.63×10^{-8} using only 87 classical and 36 quantum trainable parameters, substantially lower than classical models with comparable performance. Larger quantum models such as qq -4 underperform due to poor trainability arising from excessive expressibility for a simple solution, a phenomenon also observed in QML elsewhere [16]. Interestingly, the best hybrid model hy -10-4-2 is not a combination of the best classical cc -10-7 and quantum qq -2 models.

Figure 3 shows training loss against epochs for selected neural network models with shallow, deep or wide characteristics. Our results show that classical models train fast but with low accuracy, in contrast to quantum models which train slower but with high accuracy. Hybrid models inherit high trainability from the classical layer and high accuracy from quantum layer, the best features from each model. The exception is the deep hy -10-7-2 model (Fig. 3c), where training is weighted towards the classical layer than the quantum layer.

3.2 Discontinuous Euler

Consider a 1D Euler equation with moving contact discontinuity ([3], example 1). We use Dirichlet boundary conditions,

$$(\rho_L, u_L, p_L) = (\rho_R, u_R, p_R) = (1.0, 0.1, 1.0), \quad (12)$$

where subscripts L and R refer to left and right boundaries respectively. The exact solutions are

$$\rho(x, t) = \begin{cases} 1.4, & x < 0.5 + 0.1t, \\ 1.0, & x > 0.5 + 0.1t, \end{cases} \quad u(x, t) = 0.1, \quad p(x, t) = 1.0, \quad (13)$$

in a domain defined by $x \in (0, 1)$ and $t \in (0, 2)$. Following ([3], example 1), we randomly sample $N_{ic} = 60$, $N_{bc} = 60$ and $N_F = 1000$ training points for initial condition ic , boundary condition bc and domain F respectively.

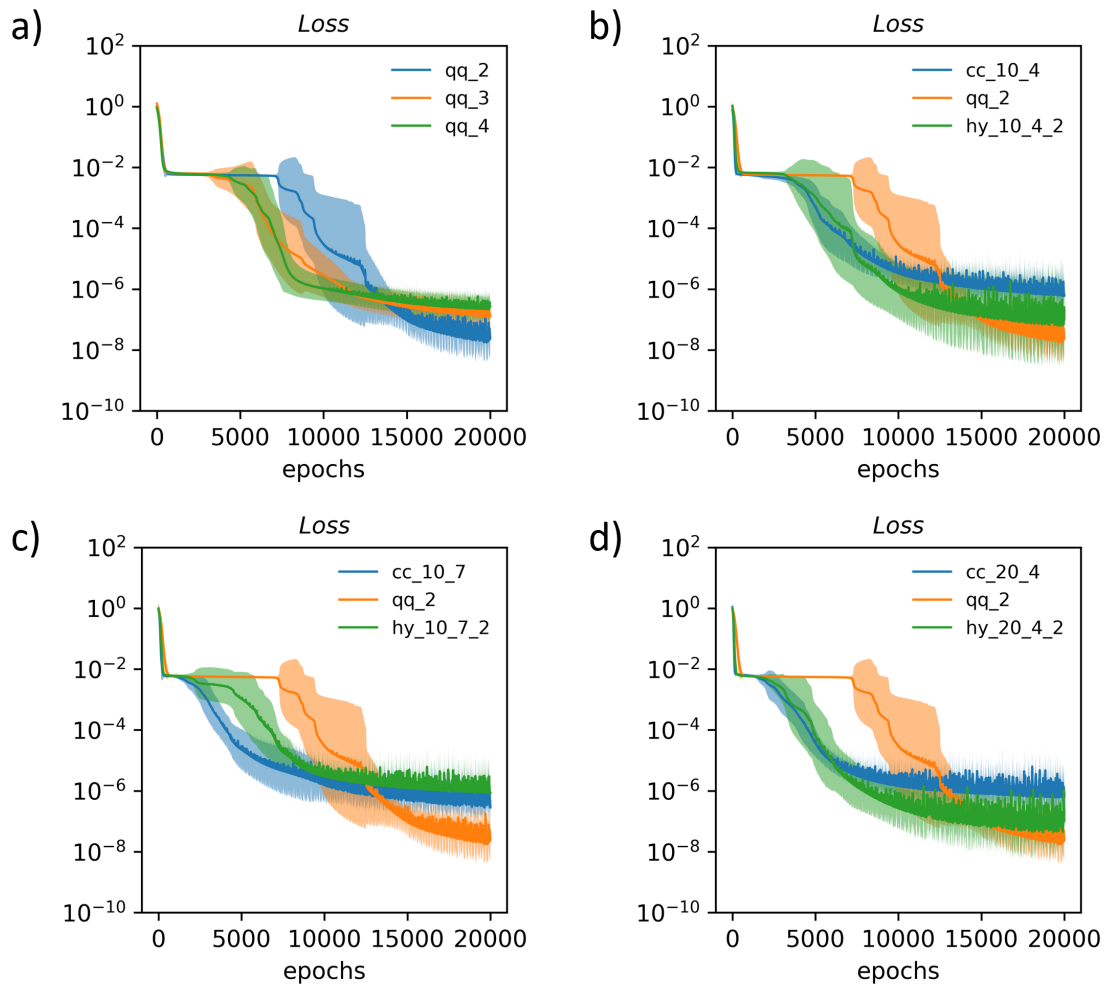


Figure 3: Training loss against epochs for smooth PINN solution of 1D Euler equation (Section 3.1). (a) Larger quantum models improve trainability at the cost of accuracy. Hybrid models outperform both (b) shallow $cc-10-4$ and (d) wide $cc-20-4$ classical models, but not (b) deep $cc-10-7$ classical model.

Model	Size	Trainable parameters	Loss	Density error	Pressure error
cc	10-4	845	6.13×10^{-7}	1.59×10^{-6}	3.28×10^{-9}
	10-7	1505	3.16×10^{-7}	7.33×10^{-7}	2.22×10^{-9}
	20-4	2845	6.65×10^{-7}	2.02×10^{-6}	3.96×10^{-9}
qq	2	87(+36)	2.63×10^{-8}	9.76×10^{-9}	1.01×10^{-9}
	3	87(+54)	1.71×10^{-7}	1.34×10^{-7}	1.87×10^{-9}
	4	87(+72)	2.75×10^{-7}	2.80×10^{-7}	2.46×10^{-9}
hy	10-4-2	448(+36)	1.98×10^{-7}	2.29×10^{-7}	8.44×10^{-9}
	10-7-2	778(+36)	3.31×10^{-7}	3.24×10^{-7}	9.04×10^{-9}
	20-4-2	1448(+36)	8.62×10^{-7}	3.19×10^{-7}	4.98×10^{-9}

Table 1: Trainable parameter count for each PINN model with additional quantum parameters in parenthesis for smooth solution problem (Section 3.1). Mean loss and relative error for density and pressure at the 20000th epoch, averaged over 6 runs. Best results shown in bold for each model.

Figure 4 shows moving contact discontinuity in the density based on classical *cc-10-4* model, where the normalized deviation from exact solution concentrated along the discontinuity itself. Table 2 compares the trainable parameters required for each model and the resultant loss and error at the 20000th epoch. Here, the best model is the shallow classical *cc-10-4* model with an average loss of 6.89×10^{-7} for 845 trainable parameters. Due to the discontinuous non-harmonic solution, the quantum *qq* models significantly underperformed compared to classical *cc* models, but improves with increasing number of trainable parameters. Overall, we find the hybrid models performed slightly worse than classical models, but significantly better than quantum models.

Figure 5 shows density profiles at time $t = 2$ where we see the quantum model fails to capture the moving contact discontinuity with an oscillatory waveform with overshoot. The hybrid model is able to correct for the perturbation error with the parallel classical layer and achieve a solution fidelity closer to that of the classical model.

Figure 6 shows training loss against epochs for selected neural network models with shallow, deep or wide characteristics. The classical models outperformed the quantum models in all cases, while the hybrid models suffer from significant variance in both trainability and accuracy in results. We find that hybrid *hy-10-4-2* and *hy-10-7-2* models are unable to match the respective classical models, especially the deep *cc-10-7* model in terms of trainability. However, the wide hybrid *hy-20-4-2* model is able to match the wide classical *cc-20-4* model, the latter likely over-parameterized.

3.3 2D Transonic Aerofoil Flow

We test HQPINN on a 2D steady Euler equation (Eq. 3) for transonic flow past an NACA0012 aerofoil with chord (0, 1) set on a square Cartesian grid $x \in (-1, 3.5)$, $y \in (-2.25, 2.25)$. Setting $U = (\rho, u, v, T)$ for density, horizontal and vertical velocities, and temperature, we apply an inlet boundary condition $U_{in} = (\rho_{in}, u_{in}, v_{in}, T_{in}) = (1.225, 272.15, 0.0, 288.15)$, outlet boundary condition $P_{out} = 0$ and periodic boundary conditions on the side boundaries, all in SI units.

The flow equations are solved using Computational Fluid Dynamics (CFD) on finite volume method with mesh refinement around the aerofoil surface and free slip boundary condition applied (refer to Appendix A.3 for details). This is followed by PINN training, where we randomly sample 40 boundary points along each boundary for data training (Eq. 6) and 4000 domain points for physics loss training (Eq. 7).

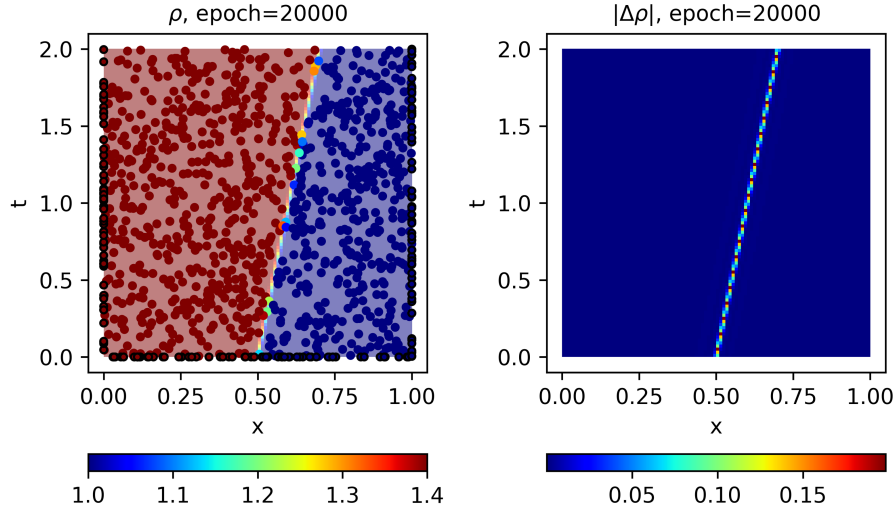


Figure 4: Plot of moving contact discontinuity for 1D Euler equation (Section 3.2). (Left) Density in x - t domain. Opaque bubbles are domain residual training points and dark circled bubbles are boundary training points. (Right) Normalized deviation from exact solution (Eq. 13).

Model	Size	Trainable parameters	Loss	Density error	Pressure error
cc	10-4	845	6.89×10^{-7}	2.89×10^{-4}	1.92×10^{-6}
	10-7	1505	1.39×10^{-6}	4.07×10^{-4}	6.06×10^{-7}
	20-4	2845	1.51×10^{-6}	4.67×10^{-4}	6.59×10^{-7}
qq	2	87(+36)	5.00×10^{-4}	1.20×10^{-3}	4.51×10^{-5}
	3	87(+54)	1.45×10^{-4}	1.30×10^{-3}	1.53×10^{-5}
	4	87(+72)	1.39×10^{-4}	9.65×10^{-4}	1.24×10^{-5}
hy	10-4-2	448(+36)	7.53×10^{-6}	5.29×10^{-4}	1.96×10^{-6}
	10-7-2	778(+36)	3.93×10^{-5}	3.55×10^{-4}	3.52×10^{-5}
	20-4-2	1448(+36)	6.98×10^{-6}	2.37×10^{-4}	3.29×10^{-6}

Table 2: Trainable parameter count for each PINN model with additional quantum parameters in parenthesis for discontinuous problem (Section 3.2). Mean loss and relative error for density and pressure averaged over 6 runs at the 20 000th epoch. Best results in bold for each model.

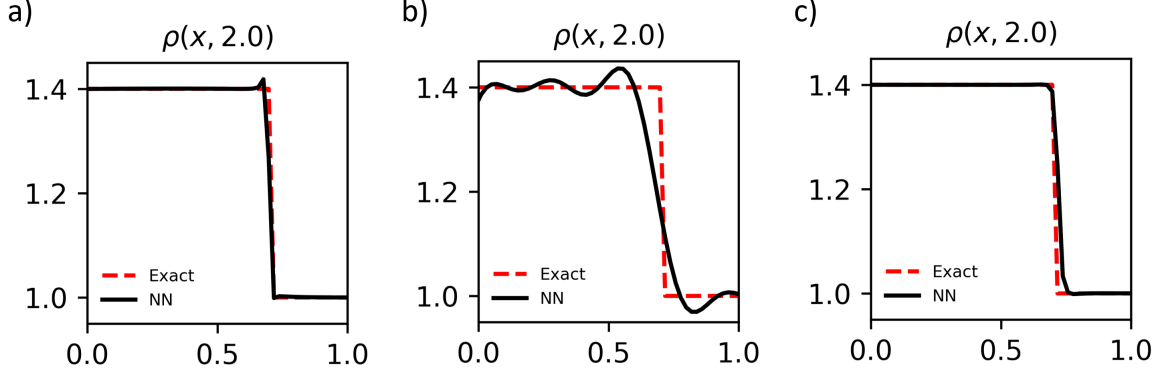


Figure 5: Density profiles at time $t = 2$ for (a) classical $cc-10-4$, (b) quantum $qq-2$ and (c) hybrid $hy-10-4-2$ models compared to exact solution (red dashed line). The quantum model (b) attempts to fit a harmonic waveform to the shock problem, leading to overshoot and under-damped oscillations; this is compensated by the hybrid model (c) due to the presence of a classical layer.

It should be pointed out that the transonic shock problem is, in fact, highly challenging even for vanilla PINNs. It is only until recently that add-on strategies, such as coordinate transformation, artificial viscosity, adaptive weights and shock sensors [22–24], enable PINNs to handle shock regions. While exploring these strategies are beyond the scope of this work, to mitigate the expression of shocks, we apply an adaptive gradient-weight [25],

$$\lambda = \frac{1}{\varepsilon(|\nabla \cdot \vec{u}| - \nabla \cdot \vec{u}) + 1}, \quad (14)$$

where \vec{u} is the velocity and ε is a parameter (here taken as 0.1). To facilitate training, we randomly assigned 400 domain points to data training instead of PDE training. Loss functions are minimized via mean square error (Eq. 6 and 7) using Adam optimizer for 40 000 steps with learning rate 0.0005, followed by L-BFGS optimizer for 2000 steps.

Figure 7 compares solutions for density, velocity and temperature for classical $cc-40-4$ model against ground solutions obtained from CFD (Appendix A.3). Solutions for quantum and hybrid models can be found in Appendix A.4. Note that the stagnation regions are small and may not resolve properly without sufficient training points sampled from within.

The transonic flow requires a minimum 40 nodes per hidden layer to resolve (Table 3). In this regard, the quantum models considered are severely under-parameterized. Yet, it is currently challenging to study the potential of larger quantum models as the time required to simulate them classically scales unfavorably, as shown by the wall time. While this bottleneck may be relieved in the future by the development of fault-tolerant quantum hardware and software acceleration, we take this opportunity to study the effects of unbalanced parameterization between the classical and quantum layers of the hybrid model.

Figure 8a show that larger quantum models do not scale well in trainability and accuracy. This may change with further increase in the number of trainable parameters. Hybrid models underperform compared to classical models (Fig. 8b-d). Unlike in the previous example (Fig. 7), hybrid models for the transonic flow problem display significantly poorer trainability compared to their classical counterparts, due to the under-parameterized quantum layer.

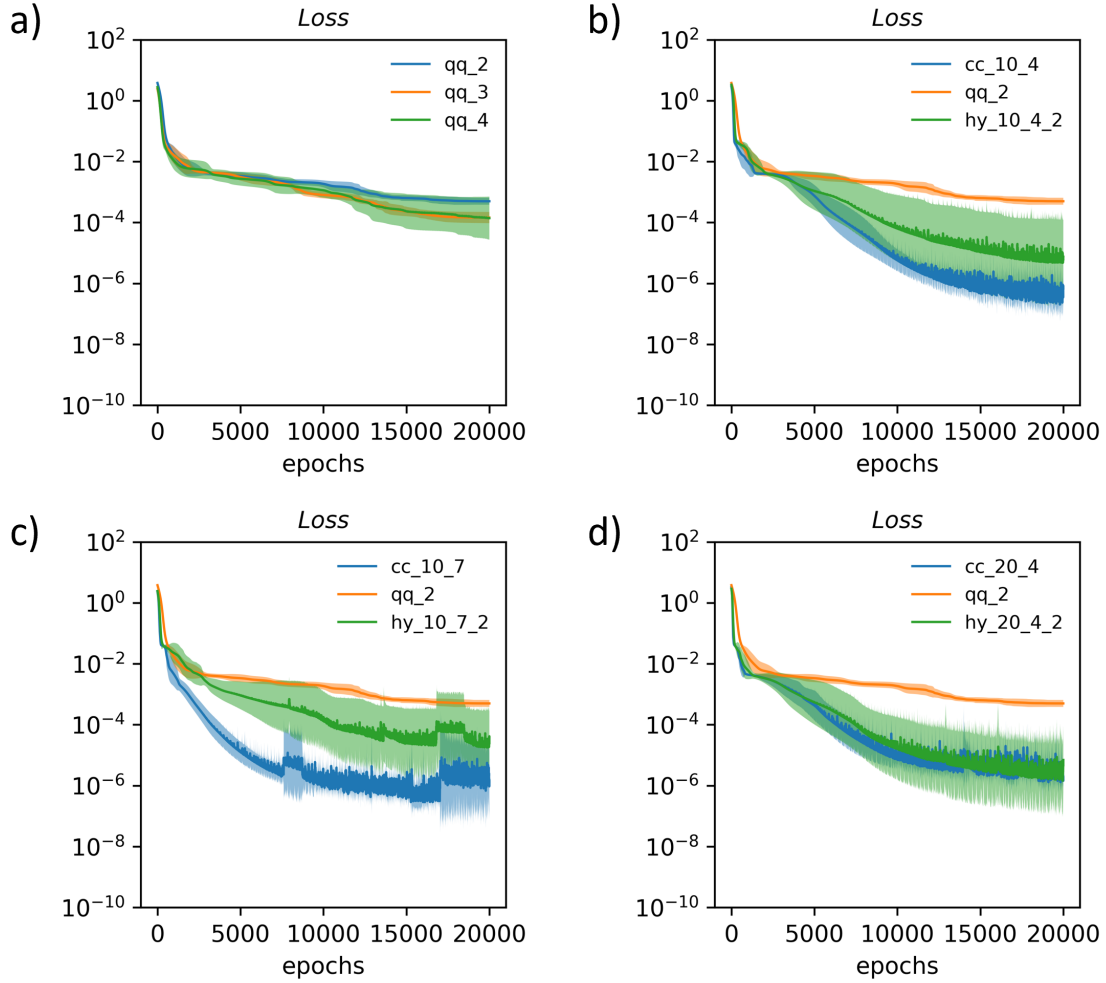


Figure 6: Training loss against epochs for discontinuous PINN solution of 1D Euler equation (Section 3.2). (a) Quantum models perform poorly for shock problems. Hybrid models outperform quantum models, but underperform (b) shallow $cc-10-4$ and (c) deep $cc-20-7$ classical models. (d) The wide hybrid $hy-20-4-2$ model is comparable to the classical $cc-20-4$ model in both trainability and accuracy.

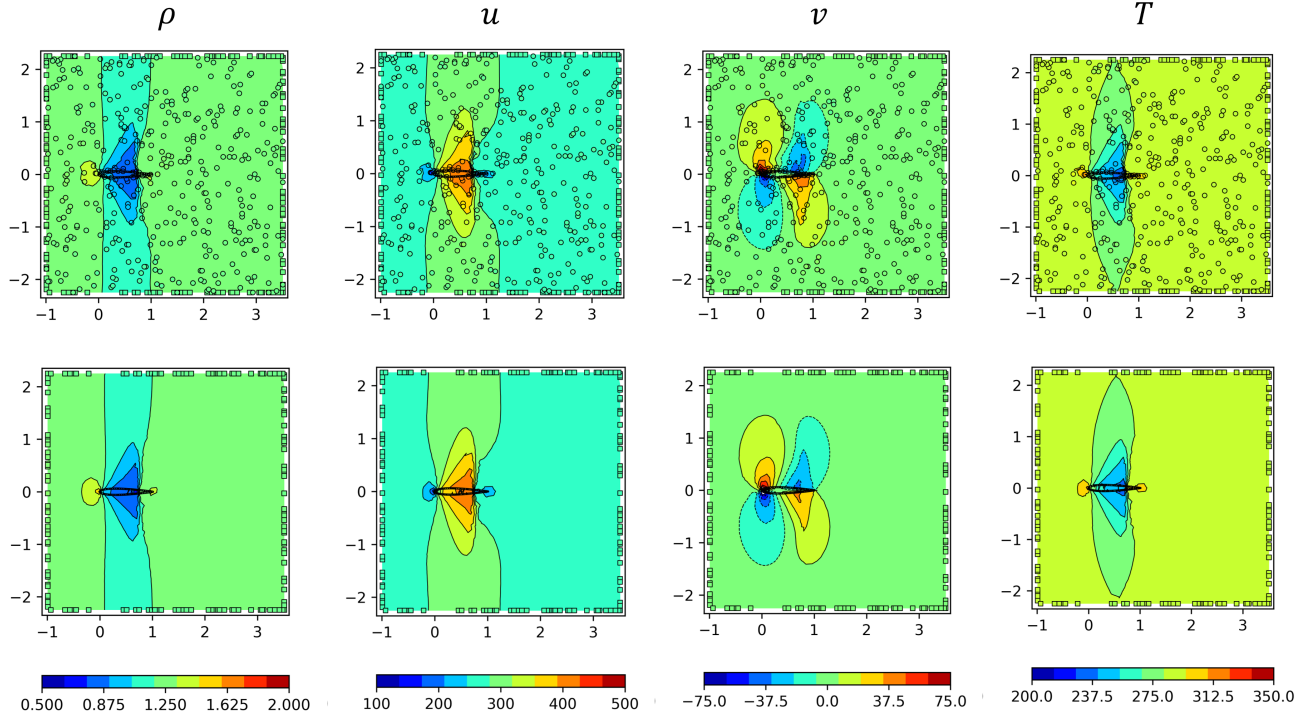


Figure 7: Solution plots of density (ρ), horizontal and vertical velocities (u, v), and temperature (T) based on (top) classical $cc\text{-}40\text{-}4$ model (training points in open circles), and (bottom) CFD solution.

Model	Size	Trainable parameters	Time (s/epoch)	Loss	Pressure error
cc	40-4	10 628	0.11	1.11×10^{-2}	1.35×10^{-3}
	40-7	20 468	0.21	2.48×10^{-3}	6.79×10^{-4}
	80-4	40 388	0.20	3.13×10^{-3}	7.74×10^{-4}
qq	2	140(+48)	1.9	9.67×10^1	3.59×10^{-3}
	4	140(+96)	4.6	8.48×10^1	2.53×10^{-3}
	6	140(+144)	9.0	6.65×10^1	4.21×10^{-3}
hy	40-4-2	5360(+48)	1.3	1.36×10^{-1}	4.05×10^{-3}
	40-7-2	10 280(+48)	1.1	3.71×10^0	1.95×10^{-3}
	80-4-2	20 240(+48)	1.1	2.56×10^{-2}	2.46×10^{-3}

Table 3: Trainable parameter count for each PINN model with additional quantum parameters in parenthesis for discontinuous problem (Section 3.3). Average wall time shown in seconds per epoch. Mean loss and relative error for pressure averaged over 6 runs at the 42000th epoch.

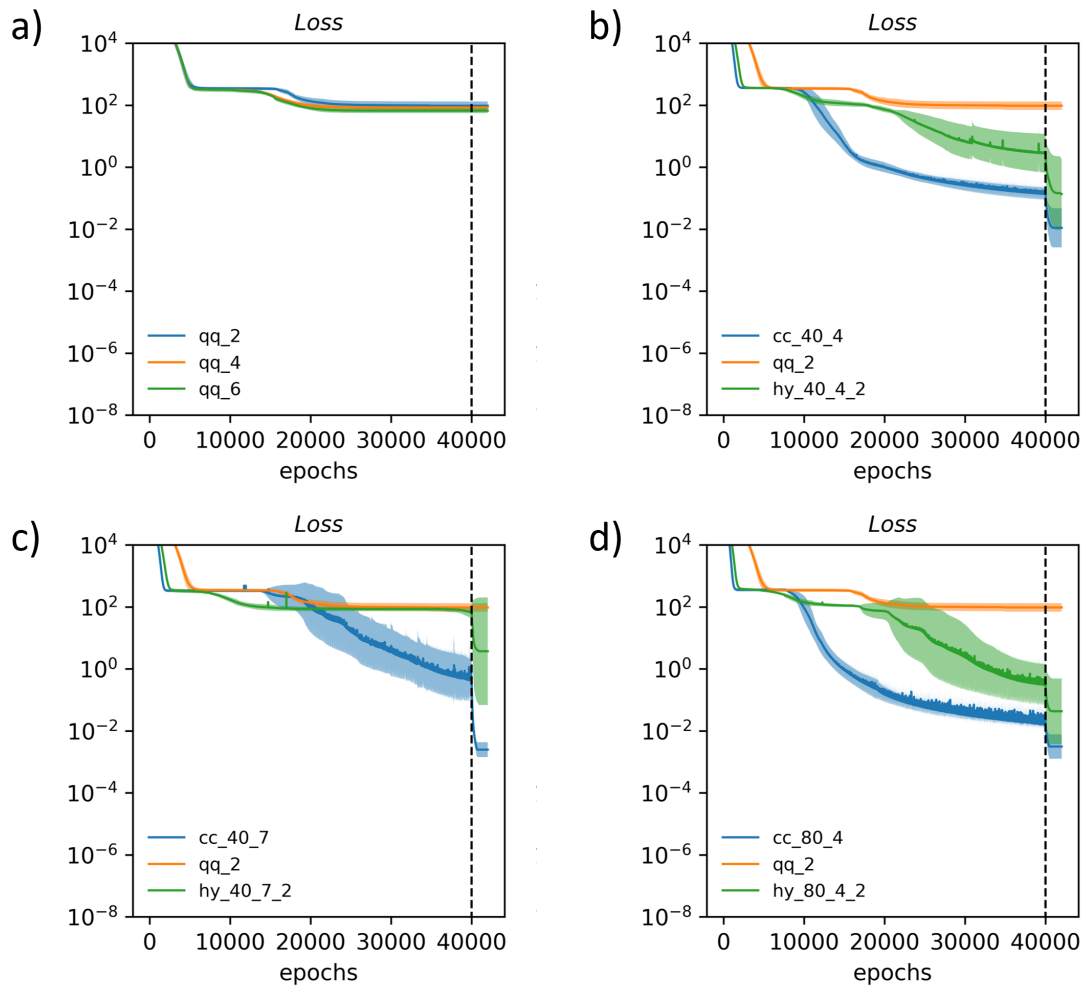


Figure 8: Training loss against epochs for PINN solution of 2D transonic aerofoil problem (Section 3.3). (a) Quantum models perform poorly for shock problems. Hybrid models outperform quantum models but underperform (b) shallow $cc\text{-}40\text{-}4$, (c) deep $cc\text{-}40\text{-}7$ and (d) wide $cc\text{-}80\text{-}4$ classical models.

Model	Harmonic		Non-harmonic		Number of trainable parameters
	Accuracy	Trainability	Accuracy	Trainability	
Classical	Medium	High	High	High	High
Quantum	High	Low	Low	Low	Low
Hybrid	Medium–High	Medium–High	Medium	Varies	Medium–High

Table 4: Qualitative assessment of PINN models in the present study.

4 Conclusion

Here we discuss the implementation of a HQPINN model for high-speed flow problems, compared to classical and quantum PINN models. A qualitative summary is provided in Table 4.

For problems with harmonic solutions (Sec. 3.1), quantum models achieve high solution accuracies using very few trainable parameters. Classical models trains faster but are less economical in parameter count. With sufficient parameterization, hybrid models may outperform both quantum and classical models (see Fig. 3d).

For problems with non-harmonic solutions (Sec. 3.2), classical models significantly outperform quantum models. Hybrid models correct for overshoot and under-damped oscillations presented by quantum models (Fig. 5), but are only intermediate in terms of accuracy as they suffer from large variance in training loss due to classical and quantum sub-models. With sufficient parameterization, hybrid models may be able to match the performance of classical models (Fig. 6d). Trainability varies from medium–high (Sec. 3.2) to low (Sec. 3.3), depending on the complexity of the problem.

In conclusion, the HQPINN excels at problems with harmonic solutions, combining the best accuracy, trainability and scalability features from both classical and quantum networks. However, the HQPINN appears ill-suited for difficult problems with shocks and discontinuous solutions, with poor trainability for more complex problems. Hybrid PINN architectures may find use in applications where the nature of the solution is not known *a-priori*. In practice, a hybrid classical-quantum architecture can be implemented in a CPU-QPU environment, leveraging the capabilities of the latest quantum chips and processors in the pipeline, such as Google’s Willow [26] and Microsoft’s Majorana I [27]. Specifically, the quantum processing unit (QPU) can efficiently process the quantum layer for harmonic components, while the CPU handles the classical layer for non-harmonic components. Future work may include adaptive weight balancing between classical and quantum sub-network layers, use of GPU-accelerated classical simulation of quantum models and fault-tolerant quantum hardware as they become available.

Acknowledgements

This research is supported by the National Research Foundation, Singapore and the Agency for Science, Technology and Research (A*STAR) under its Quantum Engineering Programme (NRF2021-QEP2-02-P03), and A*STAR C230917003.

Author Declarations

The authors have no conflicts to disclose.

Data Availability

The data that support the findings of this study are available from the corresponding author upon reasonable request.

References

- [1] D. Sandeep et al. Cfd simulation of transonic turbulent flow past naca 0012 aerofoil. *AIP Conference Proceedings*, 2316, February 2021. DOI: 10.1063/5.0036890/13880496/020013_1_ONLINE.PDF.
- [2] M. Raissi, P. Perdikaris, and G.E. Karniadakis. Physics-informed neural networks: A deep learning framework for solving forward and inverse problems involving nonlinear partial differential equations. *Journal of Computational Physics*, 378:686–707, February 2019. DOI: 10.1016/j.jcp.2018.10.045.
- [3] Zhiping Mao, Ameya D. Jagtap, and George Em Karniadakis. Physics-informed neural networks for high-speed flows. *Computer Methods in Applied Mechanics and Engineering*, 360:112789, March 2020. DOI: 10.1016/j.cma.2019.112789.
- [4] Ameya D. Jagtap et al. Physics-informed neural networks for inverse problems in supersonic flows. *Journal of Computational Physics*, 466:111402, October 2022. DOI: 10.1016/j.jcp.2022.111402. arXiv: 2202.11821.
- [5] Simon Wassing, Stefan Langer, and Philipp Bekemeyer. Physics-informed neural networks for transonic flows around an airfoil, 2024. arXiv: 2408.17364.
- [6] Wenbo Cao, Jiahao Song, and Weiwei Zhang. A solver for subsonic flow around airfoils based on physics-informed neural networks and mesh transformation. *Physics of Fluids*, 36, 2, February 2024. DOI: 10.1063/5.0188665/3267203.
- [7] Michael A Nielsen and Isaac L Chuang. *Quantum computation and quantum information*. Cambridge university press, 2010.
- [8] Abhishek Setty, Rasul Abdusalamov, and Felix Motzoi. Self-adaptive physics-informed quantum machine learning for solving differential equations. *Machine Learning: Science and Technology*, 6(1):015002, January 2025. DOI: 10.1088/2632-2153/ada3ab.
- [9] Amira Abbas et al. The power of quantum neural networks. *Nature Computational Science*, 1(6):403–409, October 2021. DOI: 10.1038/s43588-021-00084-1. arXiv: 2011.00027.
- [10] Maria Schuld, Ryan Sweke, and Johannes Jakob Meyer. Effect of data encoding on the expressive power of variational quantum-machine-learning models. *Physical Review A*, 103, 3, March 2021. DOI: 10.1103/PHYSREVA.103.032430.
- [11] Davis Arthur and Prasanna Date. Hybrid quantum-classical neural networks. In *2022 IEEE International Conference on Quantum Computing and Engineering (QCE)*, pages 49–55, 2022. DOI: 10.1109/QCE53715.2022.00023.
- [12] Mo Kordzanganeh et al. An exponentially-growing family of universal quantum circuits. *Machine Learning: Science and Technology*, 4(3):035036, September 2023. DOI: 10.1088/2632-2153/ace757. arXiv: 2212.00736.
- [13] Mo Kordzanganeh, Daria Kosichkina, and Alexey Melnikov. Parallel hybrid networks: an interplay between quantum and classical neural networks. *Intelligent Computing*, 2:1–6, January 2023. DOI: 10.34133/icomputing.0028.
- [14] Ben Jaderberg et al. Let quantum neural networks choose their own frequencies. *Physical Review A*, 109(4):042421, April 2024. DOI: 10.1103/PhysRevA.109.042421. arXiv: 2309.03279.
- [15] Alexandr Sedykh et al. Hybrid quantum physics-informed neural networks for simulating computational fluid dynamics in complex shapes. *Machine Learning: Science and Technology*, 5(2):025045, May 2024. DOI: 10.1088/2632-2153/ad43b2.
- [16] Y. Xiao et al. Physics-informed quantum neural network for solving forward and inverse problems of partial differential equations. *Physics of Fluids*, 36, 9, September 2024. DOI: 10.1063/5.0226232/20169547/097145_1_5.0226232.PDF.

- [17] Marcello Benedetti et al. Parameterized quantum circuits as machine learning models. *Quantum Science and Technology*, 4(4), 2019. DOI: 10.1088/2058-9565/ab4eb5. arXiv: 1906.07682.
- [18] Alexey Melnikov et al. Quantum machine learning: from physics to software engineering. *Advances in Physics: X*, 8(1), 2023. DOI: 10.1080/23746149.2023.2165452. arXiv: 2301.01851.
- [19] Oleksandr Kyriienko, Annie E. Paine, and Vincent E. Elfving. Solving nonlinear differential equations with differentiable quantum circuits. *Physical Review A*, 103(5):052416, May 2021. DOI: 10.1103/PhysRevA.103.052416. arXiv: 2011.10395.
- [20] Adam Paszke et al. PyTorch: An imperative style, high-performance deep learning library. *Advances in Neural Information Processing Systems*, 32(NeurIPS), 2019. arXiv: 1912.01703.
- [21] Ville Bergholm et al. PennyLane: Automatic differentiation of hybrid quantum-classical computations, November 2018. arXiv: 1811.04968. <http://arxiv.org/abs/1811.04968>.
- [22] Simon Wassing, Stefan Langer, and Philipp Bekemeyer. Physics-informed neural networks for transonic flows around an airfoil. *arXiv preprint arXiv:2408.17364*, 2024.
- [23] Xiang Ren et al. Physics-informed neural networks for transonic flow around a cylinder with high reynolds number. *Physics of Fluids*, 36, 3, March 2024. DOI: 10.1063/5.0200384.
- [24] Levi D. McClenny and Ulisses M. Braga-Neto. Self-adaptive physics-informed neural networks. *Journal of Computational Physics*, 474:111722, February 2023. DOI: 10.1016/j.jcp.2022.111722.
- [25] Li Liu et al. Discontinuity computing using physics-informed neural networks. *Journal of Scientific Computing*, 98, 1, January 2024. DOI: 10.1007/S10915-023-02412-1.
- [26] Rajeev Acharya et al. Quantum error correction below the surface code threshold. *Nature*, 638:920–926, 8052, December 2024. DOI: 10.1038/S41586-024-08449-Y.
- [27] Morteza Aghaee et al. Interferometric single-shot parity measurement in inas-al hybrid devices. *Nature*, 638:651–655, 8051, February 2025. DOI: 10.1038/s41586-024-08445-2.
- [28] So, what is a physics-informed neural network? <https://benmoseley.blog/my-research/so-what-is-a-physics-informed-neural-network/>. Accessed: April 24, 2024.
- [29] ANSYS Inc. *ANSYS Fluent User’s Guide*. ANSYS, Inc., Canonsburg, PA, release 2 edition, 2022.

A Appendix

A.1 Parameterized quantum circuit design

The performance of QML depends on the expressivity and trainability of the model [9], and even within the simple design framework of alternating feature map and ansatz layers, there are many configurations to choose from.

Following previous works[13, 16], we employ a four-qubit PQC as an entangled $RZ - RX - RZ$ gates for an ansatz layer $A(\theta)$, and a RY gates for a feature map layer $S(\varphi)$ (Fig. A1). In this study, we consider a PQC with the following gate sequence: $A - (S - A)_1 - \dots - (S - A)_{l-1}$.

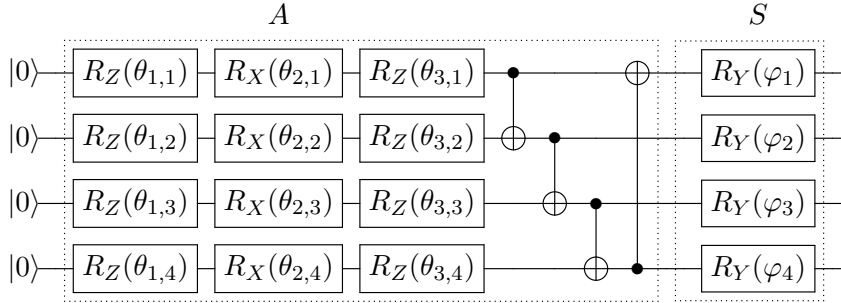


Figure A1: Example of an ansatz layer $A(\theta)$ consisting of $RZ - RX - RZ$ parameterized gate combination and $CNOT$ entanglers, and a feature map layer $S(\varphi)$ using RY parameterized gates to perform angle encoding repeated for data re-uploading. θ and φ refer to parameter weights and input features respectively.

A.2 Damped harmonic oscillator

The quantum Fourier model (Eq. 9) could extract harmonic features from a suitable dataset [13] and solve PDEs with harmonic features [16]. Here, we test the use of a hybrid classical-quantum model on a simple problem of a 1D damped harmonic oscillator, which is also an introductory PINN problem [28]. The displacement u in time t is described by a 1D second-order ordinary differential equation (ODE) as,

$$m\partial_{tt}u + \mu\partial_tu + ku = 0, \quad t \in (0, 1], \quad (15)$$

where m is the mass of the oscillator, μ is the coefficient of friction and k is the spring constant. The PINN loss function is

$$\mathcal{L} = (u_{NN}(0) - 1)^2 + \lambda_1 (\partial_t u_{NN})^2 + \frac{\lambda_2}{N} \sum_i^N ([m\partial_{tt} + \mu\partial_t + k] u_{NN}(t_i))^2, \quad (16)$$

where $u_{NN}(t)$ is neural network solution.

Following [28], we set $m = 1$, $\mu = 4$, $k = 400$, $\lambda_1 = 10^{-1}$ and $\lambda_2 = 10^{-4}$ and implement PINN on *Pytorch* [20] and *Pennylane* [21] using Adam optimizer with initial learning rate 0.002 up to 2000 epochs. The parallel neural network layers in this test are combinations of the following:

Quantum layer PQC with 3 qubits and 3 layers.

Classical layer Multi-layer perceptron with 2 hidden layers with 16 nodes each.

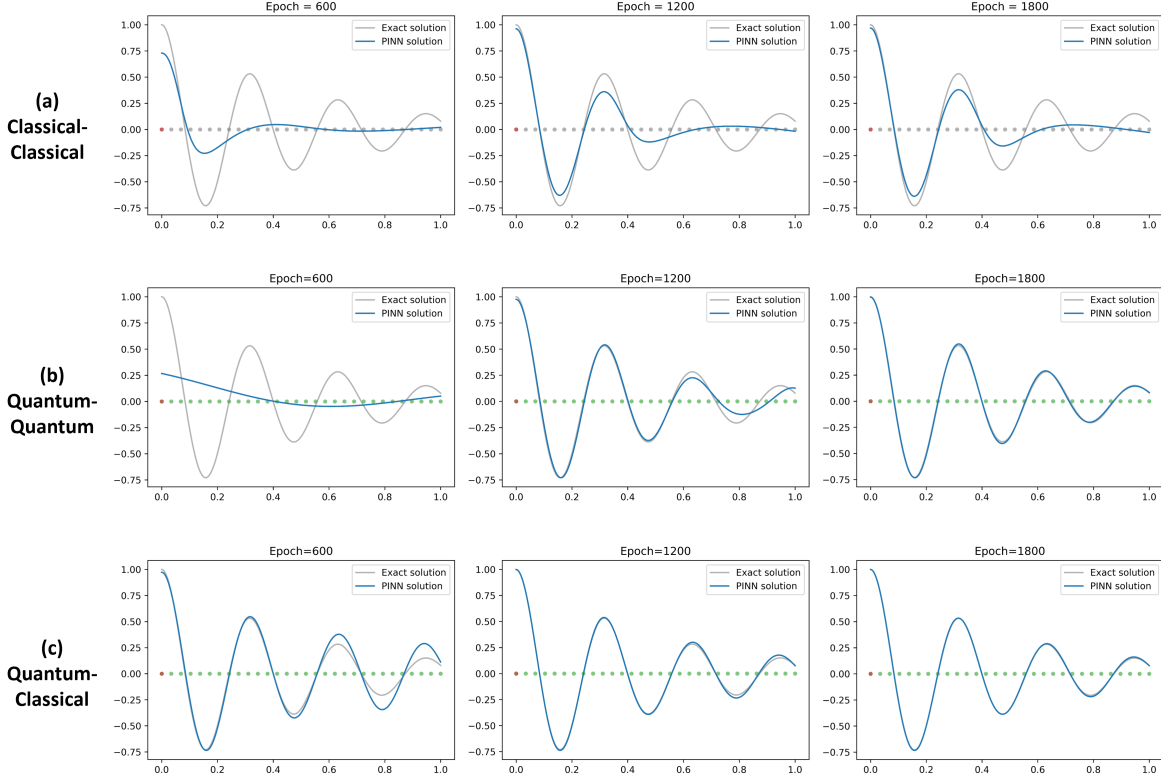


Figure A2: Plots of u_{NN} for $t \in (0, 1]$ (blue curves) compared to the exact harmonic solution (grey curves) at training times 600, 1200 and 1800 (left to right). (a) The classical–classical network responds quickly but converges poorly. (b) The quantum–quantum network (middle) responds slowly but converges strongly due to the quantum Fourier model. (c) The hybrid quantum–classical network combines training features from classical and quantum layers and is able to converge quickly and with high fidelity.

As proof of concept, we tested three parallel HQPINN configurations, namely classical–classical, quantum–quantum and hybrid quantum–classical neural networks [13]. Figure A2 shows that classical–classical networks struggles to learn the damped oscillations and requires more iterations to achieve convergence ($\approx 15,000$ epochs [28]). The quantum–quantum network converges with high fidelity, demonstrating the power of the quantum Fourier model in modeling harmonic solutions [10, 16]. Notably however, the quantum model is worse than classical model at early data fitting. By combining complementary features from classical and quantum layers, the hybrid model outperforms classical and quantum neural networks (Fig. A2c).

A.3 Computational Fluid Dynamics simulation

Computational Fluid Dynamics (CFD) simulation of steady-state transonic flow (Eq. 1 and 2) past a NACA2012 airfoil is implemented on Ansys Fluent 2022 R2 [29] using pressure-based solver on inviscid pressure-velocity coupled scheme. For spatial discretization, we apply the least squares cell-based discretization for gradients, second-order discretization for pressure, and second-order upwind discretization for density, momentum, and energy. Residual of 10^{-6} is set as the convergence criterion for all variables.

Figure A3 shows the computational domain for a 2D compressible flow over a NACA0012 airfoil with 1 m span in a 4.5 m by 4.5 m square grid. Periodic boundary conditions are applied to both the top and bottom of the domain. We specify an inlet airflow velocity at Mach number 0.8 and a temperature 288.15 K. The outlet boundary is set at null air pressure and a temperature of 288.15 K. Free slip condition is

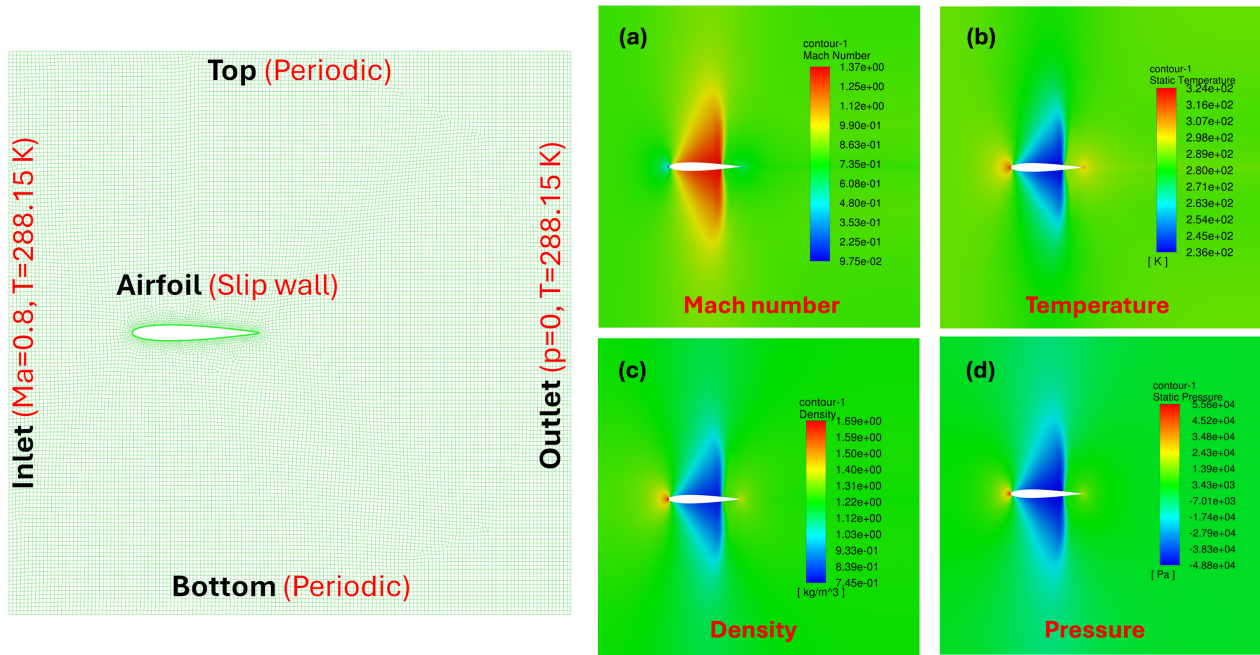


Figure A3: (Left) Computational domain for modeling a transonic flow past a NACA0012 airfoil with 1 m span in a 4.5 m by 4.5 m square grid. (Right) CFD solutions show transonic shock regions for (a) Mach number, (b) temperature, (c) density and (d) pressure.

applied at the surface of the airfoil. The finite volume grid consists of 25 000 cells with mesh refinement so that cell widths are approximately 30 mm in the domain and 10 mm near the airfoil surface.

Figure A3(a–d) illustrates the distribution of airflow properties, including Mach number, temperature, density, and pressure. The far field subsonic flow at Mach 0.8 transitions to transonic behavior as it passes over the NACA0012 airfoil, generating a normal shock near the trailing edge. Away from the stagnation region, the pressure becomes negative following momentum conservation. Both air density and temperature distributions are similar to air pressure, since they are directly proportional to pressure based on the ideal gas law.

A.4 Quantum and hybrid models for transonic flow

Here we examine sample solutions for 2D transonic flow problem (Sec. 3.3) for quantum and hybrid models (Fig. A4). The quantum model strives to fit a harmonic solution over discontinuous data training points and completely neglects vertical velocity solution due to under-parameterization. The hybrid model captures the characteristic transonic shock features using the classical network (compare Fig. 7).

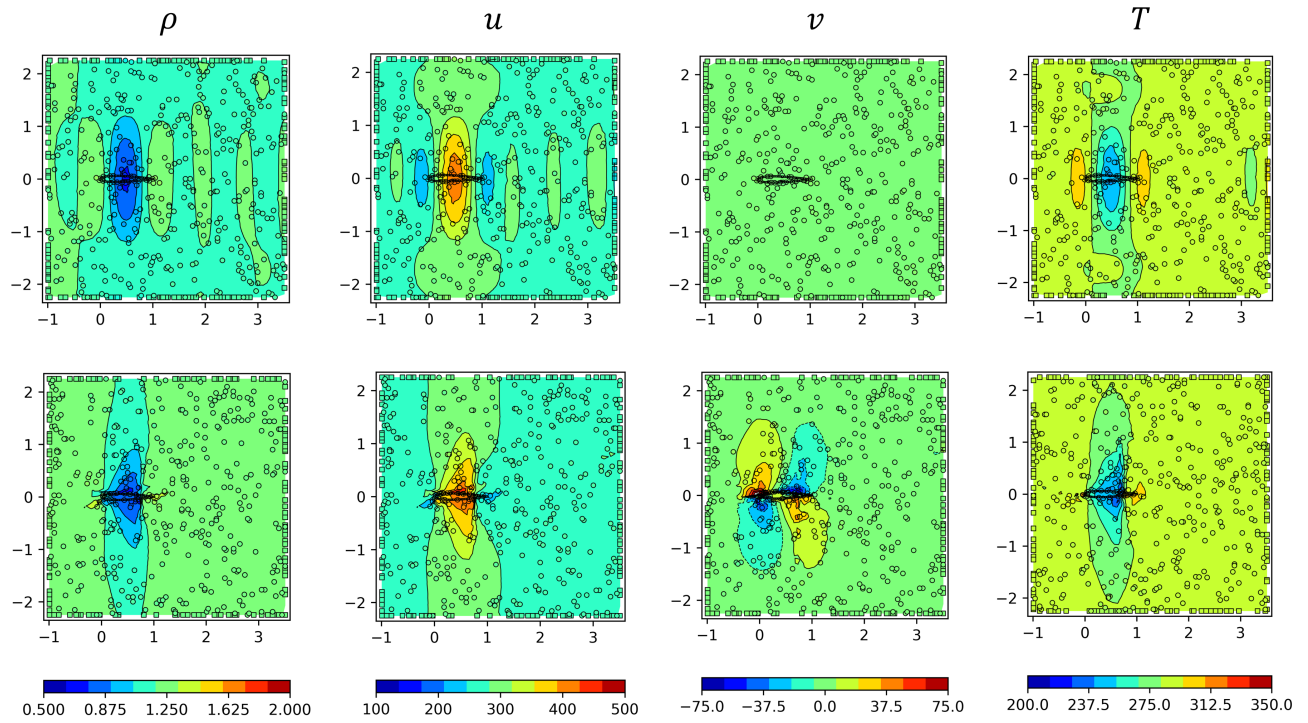


Figure A4: Solution plots of density (ρ), horizontal and vertical velocities (u, v), and temperature (T) for (top) quantum $qq-2$ and (bottom) hybrid $hy-40-4-2$ models. Training points in open circles.